Non-Invasive RF Technique for Detecting Different Stages of Alzheimer's Disease and Imaging Beta-Amyloid Plaques and Tau Tangles in the Brain

Non-Invasive RF Technique for Detecting Different Stages of Alzheimer's Disease and Imaging Beta-Amyloid Plaques and Tau Tangles in the Brain

Imran Saied, Tughrul Arslan, Siddharthan Chandran, Colin Smith, Tara Spires-Jones, and Suvankar Pal

***Abstract*— This paper describes a novel approach of detecting different stages of Alzheimer's disease (AD) and imaging beta-amyloid plaques and tau tangles in the brain using RF sensors. Dielectric measurements were obtained from grey matter and white matter regions of brain tissues with severe AD pathology at a frequency range of 200 MHz to 3 GHz using a vector network analyzer and dielectric probe. Computational models were created on CST Microwave Suite using a realistic head model and the measured dielectric properties to represent affected brain regions at different stages of AD. Simulations were carried out to test the performance of the RF sensors. Experiments were performed using textile-based RF sensors on fabricated phantoms, representing a human brain with different volumes of AD-affected brain tissues. Experimental data was collected from the sensors and processed in an imaging algorithm to reconstruct images of the affected areas in the brain. Measured dielectric properties in brain tissues with AD pathology were found to be different from healthy human brain tissues. Simulation and experimental results indicated a correlated shift in the captured reflection coefficient data from RF sensors as the amount of affected brain regions increased. Finally, images reconstructed from the imaging algorithm successfully highlighted areas of the brain affected by plaques and tangles as a result of AD. The results from this study show that RF sensing can be used to identify areas of the brain affected by AD pathology. This provides a promising new non-invasive technique for monitoring the progression of AD.**

***Index Terms*—Alzheimer's disease, dielectric measurements, medical diagnosis, microwave imaging, radio frequency**

I. Introduction

Alzheimer's disease (AD) is the most common form of neurodegenerative disease and is also the sixth leading cause of death in the United States [1]-[2]. According to the Alzheimer's Association in U.S., AD is the most expensive disease in the U.S. compared to cancer and heart disease, with cost of care totaling an estimated $290 billion in 2019 [3]. AD is also the leading cause of death in women and the second leading cause of death in men in the U.K. [4] The Alzheimer's Society in the U.K. found that there are more than 520,000 people with AD out of 850,000 suffering from dementia [5]. These numbers are expected to rise to 1 million by 2025.

Pathological changes in the brain that occur due to AD are: brain atrophy (or progressive shrinkage of the brain), particularly the hippocampus, and secondary lateral ventricle enlargement [6]. Histologically in AD the major change in the brain is the progressive accumulation of beta-amyloid plaques and tau neurofibrillary tangles [7]. Beta-amyloid proteins show up as irregular clumps in the brain that stick together to form plaques, interrupting the signals between synapses [8]. Amyloid plaques initially develop in the neocortex and spread down through the brain in a characteristic fashion very early in the disease process [9]. In addition, neurofibrillary tangles formed of intracellular aggregates of tau protein are present in large numbers in the brain as AD progresses. These tangles interfere with the transport of cell nutrients and are thought to eventually contribute to the death of the neurons [8]. Tangles initially accumulate in the trans-entorhinal cortex and spread to the hippocampus and other brain regions as disease progresses [9]. Although the clinical phenotype of AD takes decades to develop, it is difficult to definitively diagnose AD until the clinical symptoms are advanced. In addition, early diagnosis of AD is not possible with current diagnostic scans, such as computed tomography (CT) and magnetic resonance imaging (MRI) scans [10].

Beta-amyloid plaques and tau tangles are the definitive neuropathological lesions of AD [12]. As a result, researchers have focused on understanding the properties of plaques and tangles, and how they accumulate in the brain [12]-[13]. There are well-established markers of amyloid plaques using positron emission tomography (PET) scans in living people, where patients are injected with a radioactive substance that sticks to plaques and are highlighted in the resulting scan [14], and newer tau ligands are promising to track tangles in the living brain [15]. However, the high costs and invasive approach of PET scans makes it unsuitable for some to use [16]. In addition, PET scans have poor resolution, which potentially gives a misleading indication of the progression of AD pathology [8].

It is therefore of paramount importance that other properties of plaques and tangles should be investigated, specifically, its dielectric properties. The dielectric properties

I. Saied and T. Arslan are with the School of Engineering, University of Edinburgh (e-mail: Imran.Saied@ed.ac.uk, Tughrul.Arslan@ed.ac.uk).

S. Chandran, C. Smith, and S. Pal are with the Centre for Clinical Brain Sciences, University of Edinburgh (email: Siddharthan.Chandran@ed.ac.uk, Col.Smith@ed.ac.uk, Suvankar.Pal@ed.ac.uk).

T. Spires-Jones is with the Centre for Discovery Brain Sciences, and UK Dementia Research Institute, University of Edinburgh (email: Tara.Spires-Jones@ed.ac.uk).

indicate how electromagnetic fields are transmitted, absorbed, and reflected in different biological tissues [17]. These properties, the relative permittivity and conductivity, are inherent characteristics of all tissues. Understanding these properties is therefore important for dosimetry studies, optimizing wireless telecommunication devices, and designing electromagnetic (EM) or radio frequency (RF) medical diagnostic devices [18]-[19].

RF and microwave sensing technologies have been the focus of research for the past few years for medical applications. Several studies have been conducted on investigating and designing such devices for stroke and breast cancer detection. The authors have also previously investigated RF sensing for detecting brain atrophy and lateral ventricle enlargement [20]-[21]. These devices have the advantage of being low-cost, low-profile, and non-ionising; however, the translation into clinical use is still in its infancy. Several studies have also looked into dielectric properties of brain tumors and strokes; however, to the authors' knowledge, there have been no studies reported on the measurement of dielectric properties for a brain with AD. Most recently, researchers have investigated the use of implantable antennas to detect presence of beta-amyloid proteins in cerebrospinal fluid (CSF) obtained from canines [22]. However, the implantable antenna is invasive and may not be convenient for patients to use.

This paper describes the investigation and development of a novel non-invasive approach to detect and image areas of the brain affected by plaques and tangles using RF sensors, that will ultimately be used to diagnose and monitor AD. The first part of this research focused on measuring and recording dielectric properties of human brain tissues with severe AD pathology, and comparing them to dielectric properties of healthy human brain tissues. Tissue samples were taken from a patient with severe AD and measurements were obtained on the gray matter and white matter portions using a vector network analyzer (VNA), dielectric probe, and PC.

In the second part of this research, computational models were developed using measured dielectric properties of AD brain tissues to recreate different stages of AD (i.e. Mild Cognitive Impairment (MCI), Mild AD, Moderate AD, and Severe AD, respectively) inside a realistic head model. In addition, six ultra-wideband (UWB) antennas, that acted as RF sensors, were designed, optimized, and placed around the head model. Simulations were performed to investigate whether RF sensors could detect different levels of plaques and tangles in the brain based on the stage of AD.

Finally, in the last part of this research, experiments were performed using flexible textile-based RF sensors on fabricated phantoms, representing a human brain with varying levels of brain tissues affected with plaques and tangles. Data was collected from the sensors and processed using the microwave imaging via space-time (MIST) beamforming algorithm, which was originally presented in [23], but specially modified in this research to adapt to the head and reconstruct the location and volume of AD-affected brain tissues detected in the brain.

II. Materials and Methods

A. Dielectric Measurements

Post-mortem brain tissue samples from a single patient with severe AD were obtained from the Edinburgh Brain Bank and used in the dielectric measurements. A total of 10 samples were utilized in the measurements, each with a dimension of 2 cm x 1 cm x 1 cm. The samples were taken from the frontal cortex region of the brain and contained substantial amounts of beta-amyloid plaques and tau tangles, which were categorized as Braak stage C for amyloid plaques and 5 or 6 for tau tangles, and Thal phase 1, which correlates to a severe progression of AD in the patient's brain. Samples were handled inside a Category 2 biosafety cabinet in order to safely work with the samples and maintain its temperature and humidity throughout the measurements. The biosafety cabinet was equipped with temperature and humidity controllers to control the environment inside the cabinet where the samples were placed, specifically keeping the humidity low such that no moisture is generated in the samples. Measurements were taken on both the gray and white matter regions of the tissue samples in the temperature range of 12 to 18.4 °C. Fig. 1 shows a screenshot of some of the samples used for the measurements.

Fig. 1. Selection of brain tissue samples used in dielectric measurements.

Dielectric properties of the samples were determined by measuring the input reflection coefficient of the sample using the two-port VNA, HP8753C controlled by a laptop PC. Measurements were taken between 200 MHz and 3 GHz using an Agilent high-temperature dielectric probe 85070E-0020 that was connected to the VNA and used to capture dielectric properties from the samples. A GPIB connector was used to connect the VNA with the laptop, and a software associated with the dielectric probe was utilized for capturing the dielectric properties from the probe. Fig. 2 shows the complete experimental setup that was used for the dielectric measurements which included the laptop, VNA, category 2 biosafety cabinet, and the dielectric probe.

Dielectric measurements were taken 15 times at 200 evenly distributed discrete frequency points. Measurements were taken on the gray matter and white matter areas respectively. Recorded dielectric measurements of AD brain tissues at each frequency were then averaged using a built-in software and compared to those obtained from healthy brain tissue samples reported in [25] and [26]. White matter measurements obtained in [25] were between the frequency range of 10 Hz to 20 GHz and were conducted ex- vivo on tissue samples that were obtained between 24- and 48-hours post mortem.

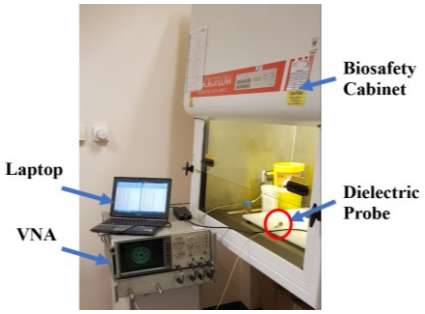

Fig. 2. Dielectric measurement setup showing the VNA, laptop, biosafety cabinet, and dielectric probe used.

The temperature of the tissue samples during the measurements were at body temperature (37℃). Gray matter dielectric measurements obtained in [26] were performed between the frequency range of 800 MHz to 2.45 GHz. The measurements were conducted on a brain specimen that was obtained from an adult human less than 10 hours after death. The measurements were performed ex-vivo and the mean temperature of the tissue during the measurements was 21.45 ± 1.6℃. Results and comparisons between the measurements performed in this study are reported in Section III-A and shown in Figs. 12 and 13.

B. Four-Pole Cole-Cole Model

Complex relative permittivity of biological tissues is frequency-dependent and characterized by the following equation [24]:

$$\varepsilon(\omega) = \varepsilon'(\omega) - j\varepsilon''(\omega) \tag{1}$$

where $\varepsilon'(\omega)$ is the real part known as relative permittivity, $\varepsilon''(\omega)$ is the imaginary part known as loss factor, and ω is the angular frequency in rad/s. The real part of (1) defines the ability of the tissue to store energy from electromagnetic fields, whereas the imaginary part indicates the dissipation of energy into heat by frictional motion of elements carrying charges [25]. As a result, the imaginary part is also related to conductivity by the following:

$$\varepsilon''(\omega) = \frac{\sigma}{\varepsilon_0 \omega} \tag{2}$$

where σ is the conductivity and ε_0 is the permittivity of free-space and equals to 8.8854×10^{-12} F/m. Dielectric properties of biological tissues are frequency dependent and vary across any given frequency range [26]. In the microwave frequency range, permittivity tends to decrease while conductivity tends to increase with respect to frequency. This variation in complex permittivity is called dispersion curve for the permittivity and absorption curve for the loss factor [24]. Typically, in order to represent the dispersion and absorption curves, the complex permittivity needs to be modeled using a dielectric model, such as the Debye or Cole-Cole model. A multi-pole or higher order model is recommended to fit the inhomogeneous and heterogeneous tissues because the single order dielectric models may not fit the complex human tissues [25]. A fourth order model is shown to provide a good fitting for tissues [26]. The four-pole Cole-Cole model for dielectric properties ($\varepsilon_C(\omega)$) is defined as:

$$\varepsilon_C(\omega) = \varepsilon_C'(\omega) - j\varepsilon_C''(\omega) = \varepsilon_\infty + \sum_{i=1}^{4} \frac{\Delta\varepsilon_i}{1 + (j\omega\tau_i)^{1-\alpha_i}} + \frac{\sigma_s}{(j\omega\varepsilon_0)} \tag{3}$$

where τ_i is the relaxation time, α_i is the exponent describing the dispersion regions, and σ_s is the static conductivity. The magnitude of the dispersion is represented by $\Delta\varepsilon_i = \varepsilon_{si} - \varepsilon_\infty$, where ε_{si} is the static permittivity when $\tau_i \ll 1/\omega$, and ε_∞ is the infinite permittivity when $\tau_i \gg 1/\omega$.

In this paper, the four-pole Cole-Cole model was used to fit the measured dielectric properties for gray matter and white matter regions of both AD and healthy tissue sample sets respectively. Estimation and optimization of the four-pole Cole-Cole model parameters were carried out using the Curve Fitting Toolbox in MATLAB. Table IV shows the list of four-pole Cole-Cole model parameters that were obtained for each of the measured sample sets.

C. Simulation Models

After obtaining the dielectric measurements, computational models were developed in CST Microwave Studio Suite. A realistic human head voxel model, initially reported in [27], was used and modified in CST. Fig. 3 shows the CST head voxel model and cross-sectional view of the head model that illustrates the different regions, tissues, and geometries that were implemented in the model.

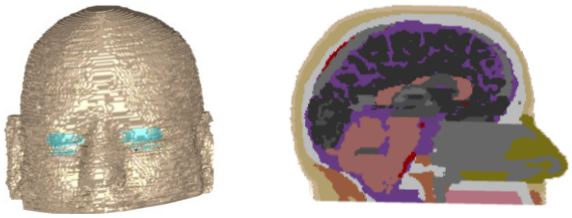

(a) (b)

Fig. 3. (a) Realistic human head model used for simulations in CST, and (b) cross-sectional view of the human head model showing the different layers, tissues and geometries of the brain.

The head model contained geometries and materials that were defined to represent different regions, tissues, and ventricles that are present in the brain. In addition, the model portrayed a realistic representation of the human head with different layers, such as skin, skull (bone), cerebrospinal fluid (CSF), gray matter and white matter. The advantage of the model was that the properties of individual areas or tissues could be controlled and modified for different conditions. The model proved to be useful in particular for defining certain areas of the brain that contain plaques and tangles during different stages of Alzheimer's disease.

In order to represent each stage of AD in the simulations, the dielectric properties of certain regions and tissues were changed to match those obtained from the dielectric measurements on the tissues. Table I lists the regions of the brain that were affected by AD in each stage and the

corresponding dataset that was used to represent the plaques and tangles. Some of the cases required both the gray matter and white matter regions to be changed as both sets of tissues were found to be affected by AD in those stages based on the work by Braak in [28].

Fig. 4 (a)-(d) shows the simulation models that were created to represent the four different stages of AD, namely mild cognitive impairment (MCI), mild AD, moderate AD, and severe AD, respectively. In addition, each of these stages, with the exception of MCI, are based on the progression and location of amyloid plaques and tau tangles in the brain as a result of AD, that was originally presented by Braak in [28]. MCI has been defined in some follow up studies [29, 30] to be the earliest known stage where plaques and tangles start to form in the hippocampus region of the brain and are characterized as either Braak stage 0, 1, 2, before spreading to other areas as mentioned in [28].

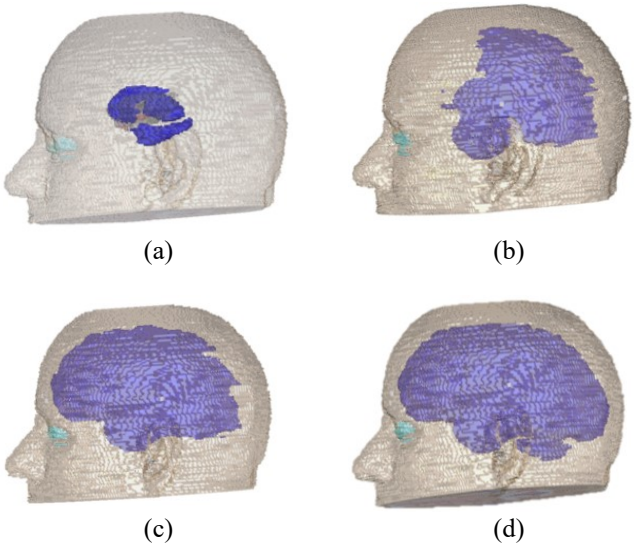

Fig. 4. Simulation models used to represent the amount of plaques and tangles (highlighted in blue) for the following stages of AD: (a) MCI, (b) Mild AD, (c) Moderate AD, and (d) Severe AD.

The RF sensor that was designed and used in the models, is an ultrawideband (UWB) antenna, with an operating frequency of 1.5 GHz that is shown in Fig. 5. A 0.1-mm-thick flexible conductive textile, Shieldex Zell is utilized as the conducting material of the sensor, while the substrate is made of RS-PRO Viscose Wool Felt material with a measured relative permittivity, ε_r and loss tangent, $tan\,\delta$ of 1.55 and 0.068 respectively. The RF sensor is fed with a microstrip line where the line is then transitioned into a stepped monopole structure. To simultaneously improve the directionality and the bandwidth of the sensor, three rectangular shaped patches of different sizes are incorporated into the design. The patches are then excited by the stepped monopole structure to yield wideband performance.

Parametric optimizations were carried out to find the optimal size of the patches. The final dimensions of the sensor are (in mm): $L = 85$, $W = 35$, $W_f = 17$, $L_{sm} = 10$, $W_{sm} = 7$, $W_{s1} = 13$, $W_{s2} = 20$, $W_{s3} = 27$, $W_{s4} = 30$, $L_t = 15$, $L_f = 12$, $L_c = 14$, $g_1 = 3$, $g_2 = 2$, $L_1 = 24$, $L_2 = 30$, $L_3 = 24$.

TABLE I
REGIONS OF HEAD MODEL USED FOR STAGES OF ALZHEIMER'S DISEASE

Stage	Brain Region Affected	Dataset Used
MCI	Medial Temporal Lobe	AD White
Mild AD	Medial Temporal Lobe	AD White
	Temporal Lobe	AD White and AD Gray
	Parietal Lobe	AD White and AD Gray
Moderate AD	Medial Temporal Lobe	AD White
	Temporal Lobe	AD White and AD Gray
	Parietal Lobe	AD White and AD Gray
	Frontal Lobe	AD White and AD Gray
Severe AD	Medial Temporal Lobe	AD White
	Temporal Lobe	AD White and AD Gray
	Parietal Lobe	AD White and AD Gray
	Frontal Lobe	AD White and AD Gray
	Occipital Lobe	AD White and AD Gray

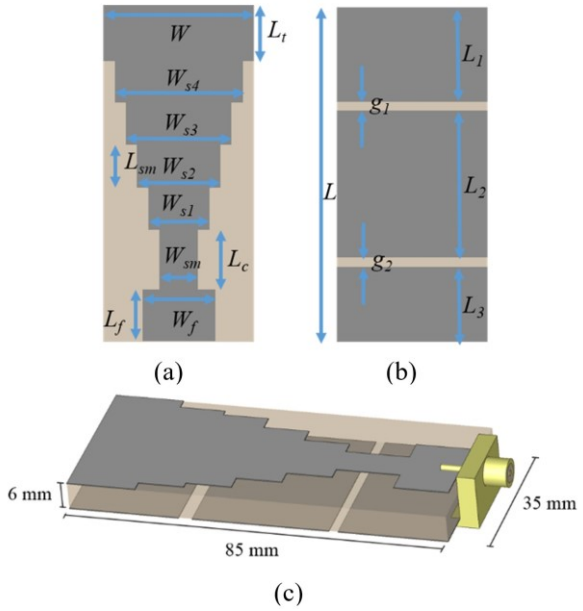

Fig. 5. Geometry of the proposed textile antenna: a) Top view, b) Bottom view, and c) Isometric view.

The intended band of operation for the sensor is between 1.3 to 4.2 GHz. The ideal operating frequency band between 1.5 and 2.1 GHz was found based on E-field distribution simulations as shown in Fig. 6. It can be observed in Fig. 6 that at 1.5 and 2.1 GHz, the proposed sensor can achieve sufficient penetration depth that allows RF waves to reach the medial temporal lobe, where early signs of AD can occur. This is different from the E-field distribution at 4 GHz, where the propagated waves can only penetrate to the gray matter layer. For considering directionality, an important factor is the front-to-back (FTB) ratio which indicates the ratio of power transmitted in the forward direction and power radiated in the backward (or opposite) direction. Although the sensor would operate mostly in near-field environment, the FTB criteria is still valid to ensure that the sensor could suppress any signals coming from its surroundings and mainly focus on the signals

coming from the head. The simulated FTB ratio of the proposed sensor at its center frequency is 6 dB, thus confirming its directional characteristic.

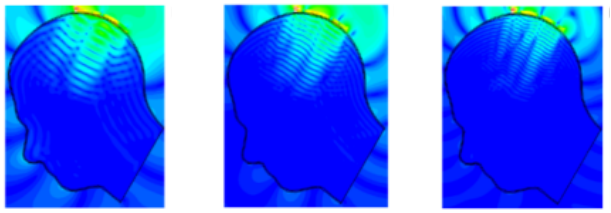

(a) (b) (c)

Fig. 6. Simulated E-field distribution of the proposed sensor inside the head at: a) 1.5 GHz, b) 2.1 GHz, and c) 4 GHz.

For the simulation model, 6 RF sensors were placed around the head model and used to capture the reflection coefficient for each area of the brain as shown in Fig. 7. For each case, S_{11} data was captured for each sensor. Then the 6 sets of S_{11} data were averaged in order to generate a mean S_{11} plot for each case and determine how the progression of plaques and tangles in the brain affects S_{11} data.

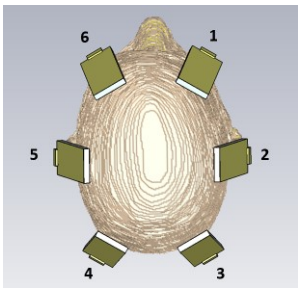

Fig. 7. Simulation model setup showing the 6 RF sensors placed around the realistic head model in CST.

D. Experimental Setup

The system setup that was used for experiments is shown in Fig. 8. The experimental setup consists of a PC, VNA, wearable textile-based RF sensors, and the skull model which contains the fabricated phantoms. Fig. 9 (a)-(b) shows the textile-based RF sensor that was used in the experiments and the hat-like structure it was integrated in. To avoid having the sensors come into contact directly with the head, another felt material was placed on the sensor to act as a superstrate. This would help to minimize errors that may occur from the presence of hair or sweat. Due to the low loss tangent of the felt material and proximity of the antenna to the head, the propagated RF waves are not affected in the near field and is found to penetrate through the skull model and into the brain.

The experiments were conducted using a host PC that was connected to the VNA via a GPIB. The PC allows the user to setup the VNA and send a command to the VNA to start generating signals and capturing S_{11} and S_{21} data from the ports directly into the PC using a built-in software. The VNA that was used for the experiments is a HP 8753 that has a frequency range of 300 kHz to 3 GHz with a dynamic range of up to 100 dB. The RF sensors were connected to the 50-ohm ports on the VNA using SMA cables.

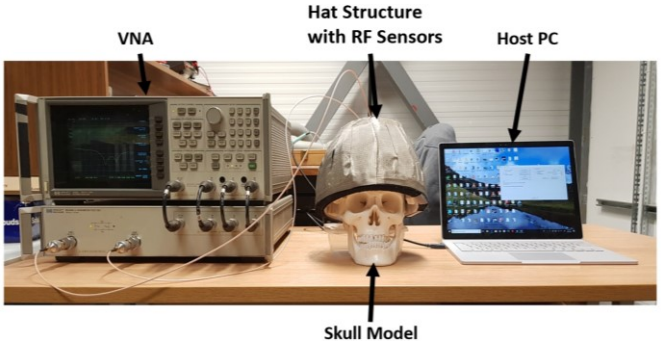

Fig. 8. Experimental setup used to test RF sensors on different levels of plaques and tangles.

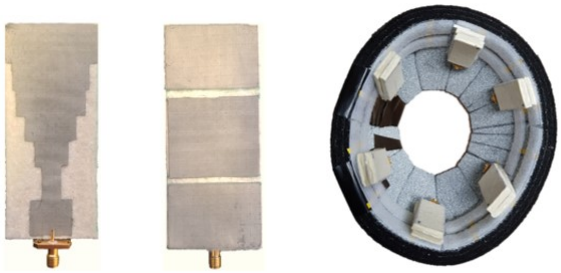

(a) (b)

Fig. 9. (a) Fabricated textile-based RF sensor used in the experiments, and (b) Hat-like structure containing the 6 RF sensors used in the experiments.

A set of artificial brain phantoms were fabricated based on a method given in [11]. Each phantom contains 3 layers: a gray matter layer, white matter layer, and a target object of varying sizes that represent AD-affected brain tissues. To recreate an artificial replica of an average adult human brain with dielectric properties of gray matter and white matter, each layer had to be fabricated separately. For the gray matter region, 1400 mL of tap water was collected. Since water has a high dielectric constant, sugar was dissolved in the water to lower the dielectric constant of the mixture. Once the ideal mixture of sugar and water was reached, the mixture was boiled with 100 g agar powder. Once boiled, the solution was poured into the skull model and left to cool for a few hours in order for the mixture to solidify. Once solidified, cutting tools were used to carve out the central part of the phantom and leave 0.8 cm of the outer layer that covers the inner side of the skull.

Next, to create phantoms representing AD-affected brain tissues, coconut oil and salt were mixed together. Dielectric properties of the mixture was measured until it reached the measured properties of AD white matter tissue samples. It was found that the dielectric property of the fabricated AD-affected phantoms was 1.08% lower than the measured dielectric properties of the AD white matter tissues across the whole frequency band, making it a suitable representation of the AD-affected brain tissues for the experiments. The mixture was then cooled in order to solidify it. After the AD-brain tissue phantom solidified, it was carefully placed in the carved-out area of the gray matter layer. Finally, the white matter layer was created using the same method for the gray matter layer, ensuring that the water and sugar mixture has a

similar dielectric property as obtained in the dielectric measurements. The mixture was then boiled with 100 g of agar and poured into the empty space inside the skull model such that it covers the AD-affected brain tissue object inside the phantom. It was then left to cool for a few hours in order to solidify and stick to the existing gray matter layer. Fig. 10 (a) shows an example of the fabricated phantoms used in the experiments and (b) shows the cross-sectional view of the fabricated phantom with the gray matter layer (blue), white matter layer (red), and embedded plaques and tangles object (white).

To ensure that the fabricated gray matter and white matter layers had the correct dielectric constant, dielectric measurements were taken for the water and sugar mixture in the liquid stage, until it was within 2% of the actual values. This is because the addition of agar had to be taken into consideration as a potential effect on the dielectric constant. Once solidified, the total volume for the phantom would equal 1400 mL, which corresponds to the total brain volume of an average adult human [10]. A final dielectric measurement was taken of the gray and white matter layers of the brain phantom after it solidified. It was found that measured dielectric properties of the fabricated gray matter phantom was 1.13% lower than those of the healthy brain tissue's gray matter region across the whole frequency band. In addition, the measured dielectric properties of the fabricated white matter phantom was 1.56% lower than those of the healthy brain tissue's white matter region across the whole frequency band. As a result, these phantoms are both suitable representations of the actual gray and white matter regions respectively. Table II below shows the composition of materials used to fabricate the phantoms. In addition, Table III provides the percentage change in the dielectric properties between the phantoms and actual tissues at certain frequency points.

TABLE II
COMPOSITION OF MATERIALS USED TO CREATE PHANTOMS

Phantom	Water (mL)	Sugar (g)	Coconut Oil (mL)	Salt (g)	Agar (g)
Gray Matter	1400	510	0	0	100
White Matter	1400	730	0	0	100
AD-Affected Tissue Object	0	0	700	60	0

TABLE III
PERCENTAGE CHANGE OF MEASURED DIELECTRIC PROPERTIES BETWEEN PHANTOMS AND ACTUAL TISSUES

Phantom	0.2 GHz	1 GHz	2 GHz	3 GHz
Gray Matter	-0.83	-1.04	-1.11	-1.2
White Matter	-1.4	-1.72	-1.34	-1.64
AD-Affected Tissue Object	-1.16	-0.89	-0.94	-1.05

In order to emulate the spread of plaques and tangles in the brain, a total of 5 phantoms were created, each with varying volumes of AD-affected brain tissue phantom embedded in the 2-layer brain phantom. The volumes of the AD-affected brain tissue phantom in each case are the following: 1) 0 mm^3 (healthy case), 2) 22.6 mm^3, 3) 56.5 mm^3, 4) 113 mm^3, and 5) 226 mm^3.

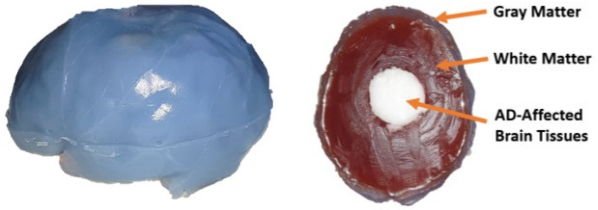

(a) (b)

Fig. 10. (a) Fabricated human brain phantom used in the experiments, and (b) Cross-sectional view of the phantom showing the gray matter (blue), white matter (red), and AD-affected tissue object (white) embedded in the phantom.

To perform the experiments, first the normal brain phantom (i.e. without the embedded AD-affected tissue objects) was inserted in the skull model and S_{11} measurements were captured for each RF sensor and averaged in order to capture the reference dataset for a model with no plaques/tangles. This reference dataset would be used later when reconstructing images for the experimental cases. Next, each of the phantom with the embedded plaques/tangles object (i.e., 22.6 mm^3, 56.5 mm^3, 113 mm^3, and 226 mm^3) is placed in the skull model. Subsequent S_{11} data was collected from each RF sensor and averaged. This data is then processed in the imaging algorithm to reconstruct the images associated with the experimental case.

E. Imaging Algorithm

After the experiments, S_{11} data was used to recreate images of AD-affected brain tissue phantoms in the skull model for each case. The imaging algorithm used in this paper was a modified version of the microwave imaging via space-time (MIST) beamforming algorithm that was presented in [23] and shown in Fig. 11.

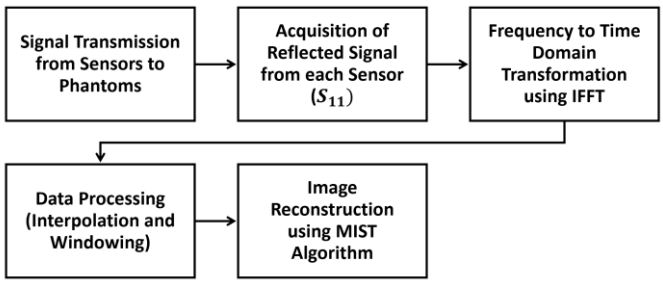

Fig. 11. Block diagram illustrating the MIST beamforming process.

In this algorithm, each antenna, or in this case, RF sensor, sequentially illuminates the head region with an UWB pulse signal and records the backscattered data. The space-time beamformer first time-shifts the returned signals to align them from a particular point in space. The time-aligned signals are then passed through a finite-impulse response (FIR) filter and summed to obtain the beamformer output. The result is time-gated and the energy for the point of interest is calculated.

In order to correctly highlight the areas of the brain containing the AD-affected brain tissues object, a reference image matrix was generated for the skull model that only contains the healthy brain phantom and no plaques/tangles objects. This image matrix is then subtracted from the image matrices generated for each experiment case to filter the data associated with the healthy brain phantom. The remaining data that is present in the image matrices therefore corresponds to the AD-affected brain tissue object that is in the skull model. An energy map is created utilizing all the beamformer outputs, further iterations are conducted to enhance the objects' image and filter noise, and the location of AD-affected brain tissues are highlighted in the resulting image.

The original MIST algorithm that was reported in [23] was used for breast cancer detection; therefore, it was not suitable to use for the purpose of head imaging due to differences in the location of the antennas used in the original algorithm, and resulting time delay that was derived. However, in order to modify this algorithm to use in head imaging, the RF sensors' location had to be updated to match with those used in the experiments, where 6 RF sensors were placed around the circumference of the head. By updating the sensors' location, the calculated time shift for each returned signal is changed to match with the distance associated with the sensor on the head. As a result of this slight modification, the modified MIST algorithm is capable of correctly aligning the backscattered signal data from the head with the correct time shift and reconstruct images in the head.

III. Results and Discussion

A. Dielectric Measurement Results

Dielectric properties of the samples were measured and compared with those of healthy human brain sample. Fig. 12 shows the plot of the relative permittivity (real and imaginary) of the gray matter region of AD-infected brain tissue as compared to those of gray matter from a healthy human brain. The mean and standard deviation of the measured datasets for gray matter are provided in Table III.

Analyzing the trends of the relative permittivity plots, there is a clear distinction between the gray matter readings from a healthy brain and a brain with AD. For instance, at 770 MHz, the real part of the relative permittivity is 56.434 for gray matter in a healthy brain and 44.89 for gray matter in the AD-infected brain, which represents a 20.46% decrease in the real part of the relative permittivity.

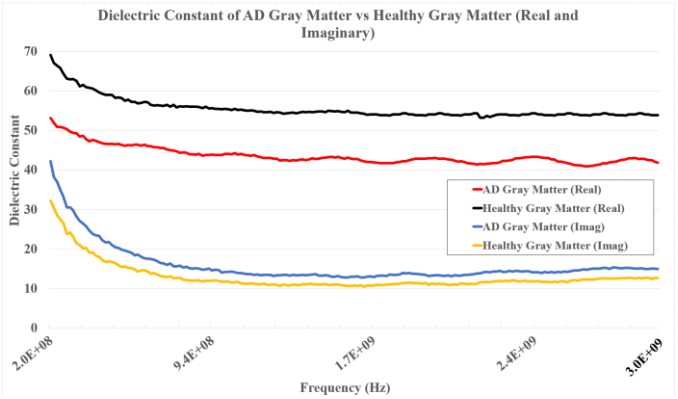

Fig. 12. Measured dielectric constant (real and imaginary) of gray matter section of AD vs. healthy human brain tissue.

At 2.4 GHz, the real part of the relative permittivity is 54.263 for gray matter in the healthy brain and 42.939 for gray matter in the AD-infected brain. The relative permittivity is slightly lower, but the percentage of change at this frequency is 20.87%, which is similar to that found in 770 MHz. It can be concluded that AD-infected brain sample has a lower relative permittivity compared to that of a healthy brain sample. In addition, it can also be seen that the imaginary part of the relative permittivity for gray matter is higher for the brain with AD compared to the healthy brain. For instance, at 2.4 GHz, there is a 16.17% increase in the value for the imaginary part of the relative permittivity for gray matter in the brain with AD.

In addition to understanding the effects of plaques and tangles on gray matter, it is also important to investigate its effects on white matter since that layer would get affected first by plaques and tangles before spreading to the gray matter layer of the brain. Fig. 13 shows the plot of measured relative permittivity (real and imaginary) for the white matter region of AD-infected brain samples and compared to the measurements for the white matter region of healthy brain tissue samples. The mean and standard deviation of the measured datasets for white matter are provided in Table V. Analyzing the relative permittivity plots in Fig. 13, a visible trend shows that there is a similar difference in the relative permittivity data across the frequency spectrum for the white matter region as in gray

TABLE IV
Four-Pole Cole-Cole Model Parameters Across 0.2 to 3 GHz

Tissue Type	ε_∞	$\Delta\varepsilon_1$	τ_1	α_1	$\Delta\varepsilon_2$	τ_2	α_2	$\Delta\varepsilon_3$	τ_3	α_3	$\Delta\varepsilon_4$	τ_4	α_4	σ_s
Gray Matter -AD	40.12	30.09	1.73e-8	0.9903	20.06	7.98e-9	0.9942	30.09	1.73e-8	0.9903	20.06	7.98e-9	0.9942	1.23e-17
Gray Matter -Healthy	34.56	34.53	1.28e-2	0.7747	34.53	1.28e-2	0.7747	34.53	1.28e-2	0.7747	34.53	1.28e-2	0.7747	1.64e-17
White Matter -AD	12.77	6.383	4.35e-14	0.9221	6.383	4.36e-14	0.9221	6.383	4.38e-14	0.9221	6.383	4.40e-14	0.9221	2.91e-18
White Matter -Healthy	22.35	12.35	3.95e-14	0.6606	12.35	3.87e-14	0.6608	0.661	3.71e-14	0.6611	12.35	3.79e-14	0.6611	4.858e-18

matter. For example, at 770 MHz the relative permittivity is 40.138 for white matter in the healthy brain and 32.32 for white matter in the AD-infected brain, which corresponds to a 19.48% decrease in the relative permittivity.

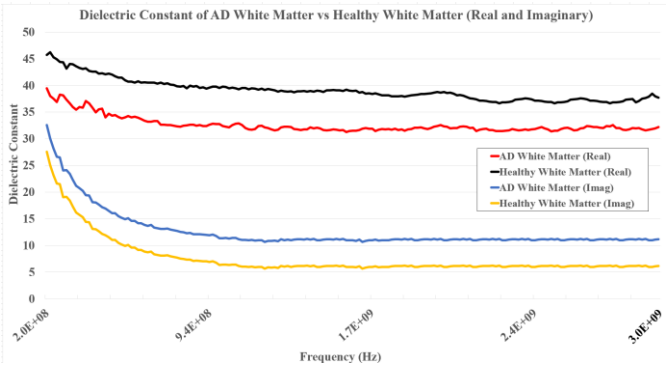

Fig. 13. Measured dielectric constant (real and imaginary) of the white matter section of AD vs. healthy human brain tissue.

TABLE V
STATISTICAL ANALYSIS OF MEASURED DIELECTRIC CONSTANTS

Tissue Type	Mean (Real)	Std. Dev. (Real)	Mean (Imag.)	Std. Dev. (Imag.)
Gray Matter -AD	43.612	±2.2700	15.9041	±4.9033
Gray Matter -Healthy	55.455	±2.7066	12.9433	±3.6475
White Matter -AD	32.610	±1.5320	12.6695	±3.841
White Matter -Healthy	39.064	±1.9958	7.6695	±3.7356

At 2.4 GHz, the relative permittivity is 37.517 for white matter in the healthy brain, and 31.824 for white matter in the AD-infected brain, corresponding to a 15.17% change. As in the plots for gray matter results, there is a decrease in relative permittivity between the healthy brain sample and AD-infected brain samples. In addition, a similar trend can be seen for the imaginary part of the relative permittivity for white matter, as in the gray matter measurements, where there is an increase in the imaginary part value for white matter in a brain with AD compared to white matter from the healthy brain. For instance, at 2.4 GHz, there is a 44.88% increase in the value for the imaginary part for white matter in the brain with AD.

In order to represent the measured dielectric properties in terms of the four-pole Cole-Cole model (Eq. 3), the Curve Fitting Toolbox in MATLAB was used to estimate and optimize all the parameters of the model to each of the 4 measured datasets (i.e., Gray Matter-AD, Gray Matter-Healthy, White Matter-AD, and White Matter-Healthy). The estimated four-pole Cole-Cole model parameters for each tissue in the measurements is given in Table IV.

B. Simulation Results for RF Sensors

Simulations for different stages of AD were also conducted and results were analyzed. Fig. 14 shows changes in S_{11} plots obtained from simulations between a healthy brain model, with a *mean* ± *standard deviation* of −6.9392 ± 5.1699, and brain models having properties of MCI, Mild AD, Moderate AD, and Severe AD as discussed in Section II-B. The reflection coefficient is a property of electromagnetic-based sensors that detects the amount of reflected electromagnetic waves that are received by the sensor.

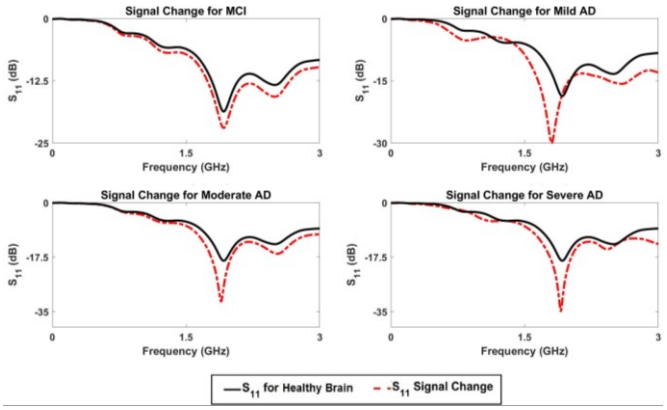

Fig. 14. Changes in S_{11} signals obtained from simulations for different stages of AD compared to S_{11} for a healthy brain.

As the disease progresses in the brain, the amount of plaques and tangles spread to other regions of the brain. This results in the S_{11} plots showing an increasing downward-shift in the reflected signal in the operating frequency range of 1.5 to 2.1 GHz, which indicates an increased loss in the signal. This is due to the dielectric changes occurring between the healthy brain and those representing different stages of AD. In particular, it can be seen that the change in S_{11} loss increases from −21.97 dB in MCI case to −34.54 dB in the Severe AD case at 1.901 GHz. In addition, it should be noted that in the case of Mild AD, where plaques and tangles affect the medial temporal, temporal, and parietal lobes, the plot shifts to the left by about 0.2 GHz. This is due to the averaged data collected from RF sensors placed around the head model. The sensors closest to the affected regions will generate higher losses, whereas those placed on the head in the frontal lobe and occipital lobe regions, will generate less loss across the frequency range, due to those regions having healthy tissues. Due to the low relative permittivity and high conductivity of brain tissues with AD, electromagnetic waves generated by the sensors are not reflected back easily as they pass through the infected areas of the brain. Instead, they tend to propagate more freely, thus causing a downward shift in the S_{11} plots. This validates the sensors' ability to differentiate different stages of AD by detecting accumulation of plaques and tangles in the reflection mode.

C. Experimental Results for RF Sensors

Experiments were performed to validate the RF sensors in detecting increasing levels of AD-affected tissues in the brain as detailed in Section II-C. The resulting S_{11} plot is shown in Fig. 15. The S_{11} plot for a healthy brain has a *mean* ± *standard deviation* of −10.0821 ± 5.9123. Results in Fig. 15 shows a similar trend found in the simulation results where the S_{11} loss increases as a result of increasing volumes of AD-affected brain tissue phantom, due to changes in the dielectric properties as a result of plaques and tangles. It can be seen that at 1.8 GHz, the change in S_{11} increases to more than double, from -19.08 dB for 22.6 mm^3 of AD-affected tissues, to -40.9 dB for 226 mm^3 of AD-affected tissues in the brain phantom.

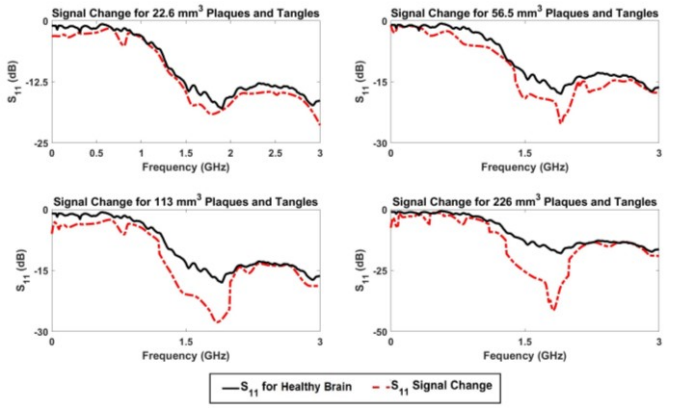

Fig. 15. Changes in S_{11} signals obtained from experiments for increasing volumes of plaques and tangles in the brain phantom compared to S_{11} with no plaques and tangles.

Similar trends can be seen in the operating frequency range of the antenna between 1.5 to 2.1 GHz, which matches the results from the simulation as well. It is also worth noting that as the AD-affected tissue volume increases inside the brain phantom, there is more change in the S_{11} loss measured outside the operating frequency range. For example, at 1.30 GHz, the change in S_{11} increases from -10.46 dB for 22.6 mm^3 to -18.62 dB for 226 mm^3 of AD-affected tissues in the brain phantom. This indicates the progression of plaques and tangles in the brain as the disease "spreads" to other regions, thus providing a promising validation of the sensors' capability in detecting and monitoring the progression of AD in the brain. The last part of this paper will utilize the measured reflection coefficient signals in the modified MIST algorithm in order to reconstruct images of the plaques and tangles in the brain phantom.

D. Image Reconstruction Results

The reflection coefficient data was collected and used as an input to the MIST algorithm that was implemented in MATLAB. Fig. 16 shows the resulting images that were reconstructed for the four different levels of plaques and tangles in the brain (i.e., 22.6 mm^3, 56.5 mm^3, 113 mm^3, and 226 mm^3 respectively).

It can be seen in the resulting images that there is a correlation between the size of the red areas, as the size of the AD-affected tissues increases. As more plaques and tangles are accumulated, the radius of the highlighted area increases as well and the central area of the affected tissues is denser (as can be seen in the dark red color in the reconstructed images, thus signifying the volume of the AD-affected tissues. The reconstructed images also show the locations of brain tissues affected by plaques and tangles accurately. The resulting images are promising and further work will be done in optimizing this algorithm and utilizing a multistatic approach to generate clearer and more accurate images from the sensors.

IV. Conclusion

Dielectric measurements were captured for AD brain tissue samples and compared with measurements from healthy brain tissue samples. Results indicate that in both gray and white matter, the accumulation of beta-amyloid plaques and tau tangles in the brain caused a shift in the real and imaginary parts of the dielectric constant. Simulations and experiments were performed to verify whether RF sensors can be used to detect different stages of AD based on the accumulation of plaques and tangles in the brain. Results confirmed that the designed RF sensors are capable of distinguishing varying levels of AD-affected tissues in the brain, due to changes in dielectric properties as a result of plaques and tangles, therefore indicating the current stage of AD in the brain. Data from the experimental results were also used in the MIST imaging algorithm to reconstruct images showing different levels of plaques and tangles in the brain. The resulting images are promising as they confirm that plaques and tangles could be detected and displayed using the data captured in the experiments. In addition, these images provide a promising non-invasive technique to detect plaques and tangles as compared to PET scans.

The results from this novel research provide a strong foundation for future work to be done in investigating how EM or RF sensing techniques can be utilized for detecting and monitoring Alzheimer's disease in a patient. In particular, comparing and validating the measurements and images generated from this technique with those obtained from functional MRIs (fMRIs) and PET scans could provide a significant opportunity in translating this novel approach as a

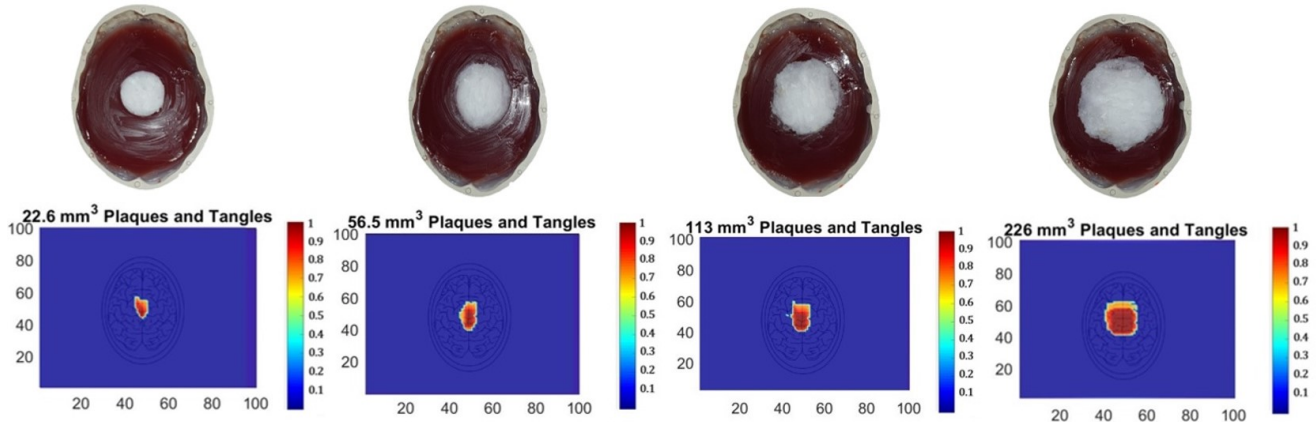

Fig. 16. Reconstructed images of the four volumes of AD-affected brain tissues in the brain phantom using the MIST algorithm (bottom row) along with the actual pictures of the objects and their placements in the brain phantom (top row).

future wearable diagnostic tool for patients with Alzheimer's disease, as well as other brain conditions, that is potentially affordable, accessible, and comfortable.

Future work will be focused on optimizing the RF sensor design and imaging algorithm further, developing more sophisticated brain phantoms that replicate the complex geometries and layers of an actual human brain, and developing more realistic experiments that emulate the different stages of AD. Factors, such as the bending of the antenna and noise in the environment, may have played a role in the measured S_{11} response in this work. These will also need to be investigated to further validate the sensitivity, accuracy, and resolution of the RF sensors and whether it is suitable for non-invasive detection and monitoring of Alzheimer's disease in the brain.

ACKNOWLEDGMENT

Use of human tissue for post-mortem studies has been approved by the Edinburgh Brain Bank ethics committee. The Edinburgh Brain Bank is a Medical Research Council funded facility with research ethics committee (REC) approval (11/ES/0022).

The authors thank the Edinburgh Brain Bank for their help and support in providing brain tissue samples and access to their labs to perform the experiments. The authors would also like to thank M. S. R. Bashri for his guidance and assistance in performing the experiments.

Finally, the authors are grateful to the family of Alasdair Sutherland for providing the Alasdair Sutherland Award to part fund the experimental work conducted in this study.

REFERENCES

[1] L. C. Walker, and H. LeVine, "The cerebral proteopathies". *Neurobiol Aging*, vol. 21, no. 4, pp. 559–561, 2000.

[2] C. A. Taylor, S. F. Greenlund, L. C. McGuire, H. Lu, J. B. Croft, "Deaths from Alzheimer's Disease-United States, 1999-2014," *MMWR Morb Mortal Wkly Report*, vol. 66, pp. 521-526, 2017.

[3] Alzheimer's Association, "2019 Alzheimer's disease facts and figures," *Alzheimer's Dementia Journal*, vol. 5, pp. 321-387, 2019.

[4] Alzheimer's Society, "What is Alzheimer's Disease: Factsheet 401LP July 2014," *Factsheet 401LP*, pp. 1-10, 2014.

[5] England and Wales; Mortality Statistics: Deaths Registered in England and Wales (Series DR). Scotland: National Records of Scotland Vital Events Reference Tables. Northern Ireland; Northern Ireland Statistic & Research Agency Registrar General Annual Report, 2017.

[6] C. Reitz, R. Mayeux, "Alzheimer disease: Epidemiology, Diagnostic Criteria, Risk Factors and Biomarkers," *Biochemical Pharmacology*, vol. 88, no. 4, pp. 640–651, 2014.

[7] C. R. Harrington, "The molecular pathology of Alzheimer's disease," *Imaging in Alzheimer's Disease and Other Demantias: Neuroimaging Clinics of North America*, pp. 11-22, 2012.

[8] C. Ballatore, V. Lee, and J. Trojanowski, "Tau mediated neurodegeneration in Alzheimer's disease and related disorders," Nat. Rev. Neurosci., vol. 8, pp. 663-672, 2007.

[9] M. Jucker and L. C. Walker, "Self-Propagation of Neurodegenerative Diseases," *Nature*, vol. 501, pp. 45-51, 2013.

[10] S. S. Rengachary and R. G. Ellenbogen, *Principles of Neurosurgery*, Edinburgh: Elsevier Mosby, 2005.

[11] A. T. Mobashsher and A. M. Abbosh, "Artificial Human Phantoms: Human Proxy in Testing Microwave Apparatuses That Have Electromagnetic Interaction with the Human Body," in *IEEE Microwave Magazine*, vol. 16, no. 6, pp. 42-62, July 2015.

[12] R. H. Takahashi, T. Nagao, and G. K. Gouras, "Plaque formation and the intraneuronal accumulation of Beta-Amyloid in Alzheimer's disease," Pathology International, vol. 67, pp. 185-193, 2017.

[13] R. Michael, A. Lenferink, G. Vrensen, E. Gelpi, R. Barraquer, and C. Otto, "Hyperspectral Raman imaging of neuritic plaques and neurofibrillary tangles in brain tissue from Alzheimer's disease patients," *Scientific Reports*, vol. 7, no. 15603, pp. 1-11, 2017.

[14] O. Sabri, M. Sabbagh, J. Seibyl, H. Barthel, H. Akatsu, et. al., "Florbetaben PET imaging to detect amyloid beta plaques in Alzheimer's disease: Phase 3 study," *Alzheimer's & Dementia*, vol. 11, no. 8, pp. 965-974, 2015.

[15] N. Okamura, R. Harada, A. Ishiki, A. Kikuchi, T. Nakamura, and Y. Kudo, "The development and validation of tau PET tracers: current status and future directions," *Clin. Transl. Imaging*, vol. 6, no. 4, pp. 305-316, 2018.

[16] M. White, N. Foster, A. Fleisher, et. al., "Clinical use of amyloid-positron emission tomography neuroimaging: Practical and bioethical considerations," *Alzheimer's & Dementia: Diagnosis, Assessment & Disease Monitoring*, vol. 1, no. 3, pp. 358-367, 2015.

[17] C. Gabriel, S. Gabriel, and E. Corthout, "The dielectric properties of biological tissues: I. Literature survey," Phys. Med. Biol., Vol. 41, pp. 2231-2249, 1996.

[18] E. Porter, H. Barami, A. Santorelli, B. Gosselin, L. Rusch, and M. Popovic, "A Wearable Microwave Antenna Array for Time-Domain Breast Tumor Screening," *IEEE Trans. Med. Imag.*, vol. 35, no. 6, pp. 1501-1509, 2016.

[19] P. T. Nguyen, A. Abbosh, and S. Crozier, "Microwave Hyperthermia for Breast Cancer Treatment Using Electromagnetic and Thermal Focusing Tested on Realistic Breast Models and Antenna Arrays," *IEEE Trans. Antennas Propag.*, Vol. 63, No. 10, pp. 4426-4434, 2015.

[20] I. M. Saied and T. Arslan, "Noninvasive Wearable RF Device Towards Monitoring Brain Atrophy and Lateral Ventricle Enlargement," in *IEEE J. Electromagn., RF, Microw. Med. Biol.*, vol. 4, no. 1, pp. 61-68, March 2020.

[21] I. M. Saied, S. Chandran and T. Arslan, "Integrated Flexible Hybrid Silicone-Textile Dual-Resonant Sensors and Switching Circuit for Wearable Neurodegeneration Monitoring Systems," in *IEEE Trans. Biomed. Circuits and Syst.*, vol. 13, no. 6, pp. 1304-1312, Dec. 2019.

[22] M. Manoufali, A. T. Mobashsher, B. Mohammed, K. S. Bialkowski, P. Mills and A. M. Abbosh, "Implantable Sensor for Detecting Changes in the Loss Tangent of Cerebrospinal Fluid," in *IEEE Trans. Biomed. Circuits Syst.,* 2020.

[23] E. J. Bond, X. Li, S. C. Hagness, and B. D. Van Veen, 2003, "Microwave imaging via space-time beamforming for early detection of breast cancer," *IEEE Trans. Antennas Propag.*, vol. 51, no. 8, pp. 1690-1705, 2003.

[24] M. Manoufali, S. A. R. Naqvi and A. M. Abbosh, "Accurate Fourth-Order Debye Model for the Head Tissues Across the 0.1–1 GHz Band Using Metaheuristic Genetic Algorithm," in *IEEE J. Electromagn., RF, Microw. Med. Biol.*, vol. 2, no. 2, pp. 79-86, June 2018.

[25] C. Gabriel, S. Gabriel, and E. Corthout, "The dielectric properties of biological tissues: II. Measurements in the frequency range 10 Hz to 20 GHz," *Phys. Med. Biol.*, Vol. 41, pp. 2231-2249, 1996.

[26] G. Schmid, G. Neubauer, and P. R. Mazal, "Dielectric properties of human brain tissue measured less than 10 h postmortem at frequencies from 800 to 2450 MHz," *Bioelectromagn.*, vol. 24, no. 6, pp. 423-430, 2003.

[27] A. Arayeshnia, A. Keshtkar and S. Amiri, "Realistic human head voxel model for brain microwave imaging," *2017 Iranian Conference on Electrical Engineering (ICEE)*, Tehran, 2017, pp. 1660-1663.

[28] H. Braak and E. Braak, "Neuropathological stageing of Alzheimer-related changes." *Acta Neuropathologica, vol. 82*, no. 4, 2015, pp. 239-259.

[29] D. Bennett, J.Scheider, J. Bienias, D. Evans, and R. Wilson, "Mild cognitive impairment is related to Alzheimer disease pathology and cerebral infarctions," *Neurology*, vol. 64, no. 5, 2005, pp. 834-841.

[30] W. Markesbery, "Neuropathologic Alterations in Mild Cognitive Impairment: A Review," *Journal of Alzheimer's Disease*, vol. 19, no. 1, 2010, pp. 221-228.